

Anomalies in Cosmic Ray Composition: Explanation Based on Mass to Charge Ratio

Adrian Hanusch*

Rostock University, Germany

E-mail: adrian.hanusch@uni-rostock.de

Tatyana Liseykina

Rostock University, Germany

E-mail: tatyana.liseykina@uni-rostock.de

Mikhail Malkov

University of California, San Diego, USA

E-mail: mmalkov@ucsd.edu

High precision spectrometry of galactic cosmic rays (CR) has revealed the lack of our understanding of how different CR elements are extracted from the supernova environments to be further accelerated in their shocks. Comparing the spectra of accelerated particles with different mass to charge ratios is a powerful tool for studying the physics of particle injection into the diffusive shock acceleration (DSA). Recent AMS-02 demonstration of the similarity of He/p , C/p , and O/p rigidity spectra has provided new evidence that injection is a mass-to-charge dependent process. We performed hybrid simulations of collisionless shocks and analyzed a joint injection of p and He^{2+} in conjunction with upstream waves they generate. By implication, our results equally apply to C and O fully ionized ions, since they have similar mass to charge ratios. By convolving the time-dependent injection rates of p and He, obtained from the simulations, with a decreasing shock strength over the active life of SNRs, we generate the integrated SNR spectra for p and He. These spectra are consistent with the AMS-02 and Pamela data and earlier theoretical predictions. Our interpretation of the elemental anomaly is therefore intrinsic to collisionless shock mechanisms and does not require additional assumptions, such as the contributions from several different SNRs, their inhomogeneous environments or acceleration from grains.

35th International Cosmic Ray Conference

10-20 July, 2017

Bexco, Busan, Korea

*Speaker.

1. Introduction

It is now well documented that the rigidity spectral indices of protons and Helium are different by ≈ 0.1 [1, 2], Fig. 1. The scaling shown in this plot is likely to continue to higher rigidities, according to other observations [3]. These findings call into question the leading hypothesis of cosmic ray (CR) origin. According to this hypothesis, they are accelerated out of an interstellar plasma of the Milky Way when it is swept by blast waves of supernovae.

The CR acceleration mechanism is believed to be electromagnetic in nature. Particles gain energy while being scattered by converging plasma flows upstream and downstream of a supernova remnant (SNR) shock. The mechanism was originally proposed in 1949 by Fermi [4] and actively researched under the name diffusive shock acceleration (DSA). It is not difficult to see that even a small, e.g., a ≈ 0.1 , difference in the rigidity spectral indices of different elements may seriously undermine any (not only the DSA!) electromagnetic acceleration mechanism. It is sufficient to write the particle equations of motion in terms of their rigidity, $\mathcal{R} = \mathbf{p}c/eZ$, instead of momentum \mathbf{p} (Z is the charge number):

$$\frac{1}{c} \frac{d\mathcal{R}}{dt} = \mathbf{E}(\mathbf{r}, t) + \frac{\mathcal{R} \times \mathbf{B}(\mathbf{r}, t)}{\sqrt{\mathcal{R}_0^2 + \mathcal{R}^2}}, \quad (1.1) \quad \frac{1}{c} \frac{d\mathbf{r}}{dt} = \frac{\mathcal{R}}{\sqrt{\mathcal{R}_0^2 + \mathcal{R}^2}}. \quad (1.2)$$

The electric, $\mathbf{E}(\mathbf{r}, t)$, and magnetic, $\mathbf{B}(\mathbf{r}, t)$, fields here are arbitrary. So, the equations apply to the CR acceleration in an SNR shock, propagation through the turbulent interstellar medium (ISM), and eventual escape from the Milky Way. It follows that all species with $\mathcal{R} \gg \mathcal{R}_0 = Am_p c^2 / Ze$ (A is the atomic number and m_p - proton mass, so $\mathcal{R}_0 \simeq A/Z$ GV) have nearly identical orbits in the phase space $(\mathbf{r}, \mathcal{R})$. If, say, protons and helium atoms are already accelerated to $\mathcal{R} = \mathcal{R}_1 \gg \mathcal{R}_0$ with a stationary p/He ratio, this same ratio will persist for all $\mathcal{R} \gg \mathcal{R}_0$, in apparent contradiction with Fig. 1.

Three different ideas have been entertained to explain the above paradox: (1) contributions from several SNRs with different p -He mixes and spectral slopes; (2) CR spallation in the ISM that introduces particle sources and sinks in Eq. (1.1); (3) shock evolution in time. The latter is the case, but this scenario is difficult to defend. Assuming the p/He ratio fixed at some fiducial rigidity $\mathcal{R} = \mathcal{R}_1 \gg \mathcal{R}_0$, it must increase while the shock strength naturally decreases. While not impossible, the p/He increase must occur at a rate consistent with the observed p/He slope in rigidity. The crucial point here is that the power-law index of shock-accelerated particles, q , decreases with the Mach number $M(t)$ in a fully determined way:

$$q = -d \ln f / d \ln \mathcal{R} = 4 / (1 - M^{-2}), \quad (1.3)$$

where f is the CR distribution function. Therefore, to reproduce the 0.1 index difference between p and He correctly, the p/He ratio at $\mathcal{R} = \mathcal{R}_1 \gg \mathcal{R}_0$ must depend on the shock Mach number in a specific way. This dependence, in turn, is an intrinsic property of collisionless shock and cannot be adjusted to fit the data, thus making the scenario (3) fully testable.

Unlike the scenario (3) above, (1) is not testable because the individual properties of contributing sources are unknown. Besides, it will likely fail the Occam's razor test, especially after the AMS-02 has measured p/C and p/O ratios to be identical to those of p/He [5]. It was also

pointed out in [6] that it would be impossible to maintain the spectral slopes in these ratios nearly constant over an extended rigidity range. Meanwhile, according to [7], the spallation effects (2) cannot fully explain the p/He rigidity dependence, either. It follows that the time dependence of the subrelativistic acceleration phase (injection into DSA, option 3 above) is the most realistic scenario to consider.

The time dependence of particle acceleration at an SNR shock comes in two flavors. Firstly, the medium into which the shock propagates may be inhomogeneous [8] (effect of SNR environment). If also the background p/He ratio increases outward, this ratio will decrease with rigidity after the acceleration, since higher rigidities are dominated by earlier times of acceleration history when the He contribution was higher. Secondly, the shock weakening (decrease of the shock Mach number) also makes the acceleration time dependent. The primary problem with the environmental explanation is that not only the He concentration must be *assumed* to decrease with growing shock radius at a specific rate (one free parameter), but also the carbon and oxygen concentrations must decrease at the same rate (two more free parameters). This conclusion follows from the C/He and O/He flux ratios being independent of rigidity [5]. So, He, C, and O are likely to share their acceleration and propagation history. One corollary of this is that C and O are unlikely to be pre-accelerated from grains, contrary to some earlier suggestions [9]. Moreover, the equivalence between the He, C and O spectra corroborates the conclusion [7] that spallation effects are insufficient to account for the observed differences in rigidity spectra between p and elements whose A/Z values are similar but higher than that of the protons. Note that it is crucial to use the rigidity dependence of the *fractions* of different species as a primary probe into the intrinsic properties of CR accelerators. Unlike the individual spectra, the fractions are unaffected by the CR propagation, reacceleration, and losses from the galaxy, as long as the spallation is negligible.

Besides being in tension with the AMS-02 recent results, the mechanisms considered so far require special conditions, such as how the CR sources are distributed in the ISM, types of supernova progenitors, or their environments. The question is then if a shock can modify an element abundance at higher energies by selectively accelerating it out of a homogeneous background plasma with no additional assumptions? It has been argued in [10] that such elemental selectivity of the initial phase of the DSA (injection) must, indeed, occur in quasi-parallel shocks. The efficiency of injection mechanism was shown to have the following properties: it depends on the shock Mach number; its efficiency increases with A/Z , then saturates at a level that grows with M . These properties have been established by analytic calculations of ion injection into the DSA [11, 10, 12].

The publication of high-precision measurements of p/He ratio by the Pamela collaboration [1], prompted the authors of [13] to apply the analytic injection theory to the case $A/Z = 2$ (specifically to He^{2+} , also valid for fully stripped C and O, accurately measured later by AMS-02). These calculations produced an excellent fit to the Pamela data in the relevant rigidity range $2 < \mathcal{R} < 200\text{GV}$. Note that lower rigidities are strongly affected by solar modulation, while at higher rigidities the Pamela statistics was insufficient to make a meaningful comparison.

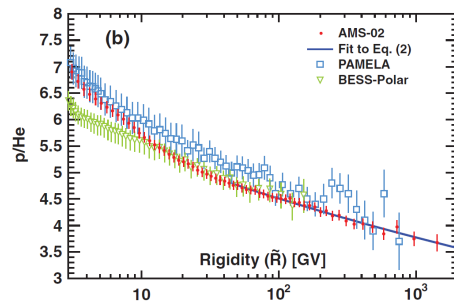


Figure 1: The p/He ratio as a function of particle rigidity. The plot is adopted from [2].

2. Analysis

The purpose of this paper is to demonstrate that the recent high-precision measurements of elemental spectra with different A/Z are not only consistent with the hypothesis of CR origin in the SNR, but also strongly support it. Although a similar stand has been taken in [13] about the Pamela findings [1], the new AMS-02 data and recent progress in shock simulations allow us to establish crucial missing links in the CR-SNR relation. In particular, the coincidence in accelerated particle spectral slopes of now three different elements with $A/Z \simeq 2$ (He, C, and O) points to an intrinsic, A/Z -based element selection mechanism and rules out incidental ones, such as those based on inhomogeneous, incompletely ionized, or dusty shock environments. Note that the latter mechanism was justified by integrated element abundance, whereas the individual rigidity spectra have become known only now.

On the theoretical side, the p/He calculations in [13] have been based on an analytic theory that allows some freedom in choosing seed particles for injection [11]. These aspects have been recently discussed, along with the limitations of hybrid simulations in [6]. Nevertheless, simulations can remove many uncertainties in the analysis, thus greatly improving our understanding of the A/Z selectivity. This will be clear after the following short discussion of self-regulation and elemental selectivity of injection.

Injected protons drive unstable Alfvén waves in front of the shock. These waves control the injection of all particles by regulating their shock crossing needed to gain energy. Proton-driven waves trap them most efficiently. Furthermore, the waves are almost frozen into the local fluid so, when crossing the shock interface, they trap most particles and prevent them from escaping upstream, thus significantly reducing their odds for injection. Again, most efficient is namely the proton trapping, while, e.g., He^{2+} ions have better chances to escape upstream and be injected. The trapping becomes naturally stronger with growing wave amplitude that also grows with the Mach number. This trend is more pronounced for the protons than He, which is crucial for the injection selectivity.

Another limitation that we remove using hybrid simulations concerns treating He ions as test particles. Several hybrid simulations, addressing the acceleration efficiency of alpha particles, did include them self-consistently [14, 15] while other considered them as test particles, e.g. [16]. The fully self-consistent simulations, however, do not provide sufficiently detailed Mach number scans of the p/He injection ratio to test the injection bias mechanism discussed earlier. Although the test particle approximation is often considered to be sufficient because of the large ($\simeq 10$) p/He density ratio, the He ions drive resonant waves that are typically two times longer than the waves driven by the protons. In the wave-particle interaction, the resonance condition is often more important than the wave amplitude. In addition, the rational relation between the respective wave lengths (2:1) is suggestive of parametric interactions between them. Such interaction should facilitate a cascade to longer waves which are vital for the DSA, not just for particle injection. To conclude this section, a state-of-the-art self consistent simulation is required to test the theoretically predicted p/He injection bias.

3. Simulations

We investigate particle injection into the DSA using hybrid simulations, whereby electrons are treated as a massless fluid. This technique is justified because the relevant scales are determined by the ions. The electron fluid is described by the following equation

$$0 = -en_e \left(\mathbf{E} + \frac{1}{c} \mathbf{v}_e \times \mathbf{B} \right) - \nabla p_e + en_e \eta \mathbf{J}, \quad (3.1)$$

where $-e$, n_e , and \mathbf{v}_e , are the electron charge, density and bulk velocity. \mathbf{E} , \mathbf{B} , and \mathbf{J} are the electric field, magnetic field, and total current. The electron pressure p_e and the resistivity η are both assumed to be isotropic, i.e., scalar quantities. The electron pressure is related to their density, n , by an adiabatic equation of state, $p_e \sim n^{\gamma_e}$, with the index $\gamma_e = 5/3$. The ions are treated kinetically as macro-particles, whose motion is governed by Newton's equations

$$m_i \frac{d\mathbf{v}}{dt} = q_i \left(\mathbf{E} + \frac{1}{c} \mathbf{v} \times \mathbf{B} - \eta \mathbf{J} \right) \quad \text{and} \quad \frac{d\mathbf{x}}{dt} = \mathbf{v}, \quad (3.2)$$

where m_i and q_i are the ion mass and charge, respectively. Eqs. (3.1) and (3.2) are non-relativistic, as $|\mathbf{v}| \ll c$ holds during the injection phase. The electric field is calculated from Eq. (3.1) using the ion density n_i and current \mathbf{J}_i obtained from particle orbits. The total current is, in turn, obtained from Ampere's law in magnetostatic approximation, while the magnetic field evolves according to Faraday's law

$$\nabla \times \mathbf{B} = \frac{4\pi}{c} \mathbf{J} \quad \text{and} \quad \frac{1}{c} \partial_t \mathbf{B} = -\nabla \times \mathbf{E}. \quad (3.3)$$

In the simulations, lengths are given in units of c/ω_p , with $\omega_p = \sqrt{4\pi n_0 e^2/m_p}$ being the proton plasma frequency, where n_0 is the upstream density and e and m_p are the charge and the mass of the proton, respectively. Time is measured in the units of inverse proton gyrofrequency, ω_c^{-1} , with $\omega_c = eB_0/m_p c$. Here B_0 is the magnitude of the background magnetic field, and the velocity is normalized to the Alfvén velocity $v_A = B_0/\sqrt{4\pi n_0 m_p}$.

In our simulations we use a realistic composition of the plasma consisting of 90% p and 10% He^{2+} in number density. Hence, the helium ions cannot be regarded as test particles. Furthermore, the simulations are one-dimensional spatially, but all three components of the fields and velocity are included. The reduced number of dimensions allows us to increase the number of waves and particle statistics, both being crucial for an adequate description of the downstream thermalization process. It requires a well-developed wave turbulence to ensure strong wave-particle interactions with extended resonance overlapping. These conditions are key to the entropy production, e.g. [17], not easy to meet in simulations. They are arguably more important than, e.g., possible shock rippling effects, not captured by 1D simulations. At the same time these, and other phenomena occurring at the shock ramp cannot be accurately characterized

v_0/v_A	$L_x/(c/\omega_p)$	$t_{\text{max}}/\omega_c^{-1}$
3	7200	3500
4	7200	2450
5	7200	1950
7	9600	1750
10	9600	1700
15	9600	1500
20	12000	1000
25	14400	1000
30	17280	750

Table 1: Size of the simulation box and duration of the simulation for different initial velocities v_0 . For the low- M shocks it takes longer until the energy spectra are converged, hence longer runs are necessary.

within hybrid simulations anyway as they require a full kinetic treatment [18, 19] (for further recent discussion of the relevant simulation aspects see [6]).

The shock simulation is initiated by sending a supersonic and superalfvénic plasma flow with velocity $v_0 > c_s \approx v_A$ against a reflecting wall. The shock forms due to the interaction of the emerging counter-propagating streams. The background magnetic field is set parallel to the shock normal $\mathbf{B}_0 = B_0 \mathbf{x}$. The upstream plasma betas are set to $\beta_e = \beta_i = 1$. The simulation box has a length of $7200 - 17280 c/\omega_p$, depending on the initial velocity v_0 (see Tab. 1). The grid spacing is $\Delta x = 0.2 c/\omega_p$ with 100 particles per cell for each species and the time step is chosen to be $\Delta t = 0.01/(v_0/v_A) \omega_c^{-1}$. All numerical parameters have been checked for convergence.

4. Results

4.1 injection efficiency

To investigate the elemental selectivity of the injection mechanism, we determine the injection efficiency of each particle species (p and He^{2+}) included in the simulation. We obtain the energy spectra of all particles downstream of the shock transition from the simulation using a logarithmic binning procedure. Energy is measured in units of $E_0 = \frac{1}{2} m_p v_A^2$. In general, the spectra of both particle species exhibit the same main features—a Maxwellian distribution and a power-law tail (see Fig. 2)—where the He^{2+} energy spectrum is shifted towards higher energies. This shift is a result of the higher He mass under velocity (not energy) randomization occurring upon crossing the shock. Additionally, a contribution of supra-thermal particles obscures the transition from the Maxwellian to the power-law making it difficult to determine the injection efficiency directly. Hence, we fit a thermal distribution $f_{\text{th}} = a E^{1/2} \exp(-E/T)$, where T is the downstream temperature of the plasma as well as a power-law with a cut-off, $f_{\text{pow}} = b E^{-q} \exp(-E/E_{\text{cut}})$, where E_{cut} is the cut-off energy.

As expected, the temperature of the He^{2+} ions is approximately four times the proton temperature and the time needed for thermalization is longer for the heavier ions. The injection efficiency is then calculated using the fits mentioned earlier, as

$$\eta_{\text{inj}} = \frac{f_{\text{th}}(E_{\text{inj}})}{\int_0^\infty f_{\text{th}}(E) dE} \quad (4.1)$$

with E_{inj} defined from $f_{\text{th}}(E_{\text{inj}}) = f_{\text{pow}}(E_{\text{inj}})$.

We have performed a number of simulations for a range of different initial upstream flow velocities v_0 (see Tab. 1), corresponding to different shock Mach numbers, $M = (v_0 + v_{sh})/v_A$, where v_{sh} is the shock velocity in the downstream (simulation) rest frame. After the energy spectra are converged, we apply our method of calculating the injection efficiency at multiple times in a time interval of $250 \omega_c^{-1}$ and compute the average. The resulting values of $\eta_{\text{inj}}^\alpha(M)$ are depicted in Fig. 3.

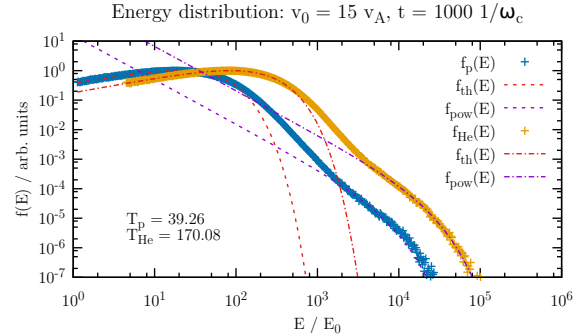


Figure 2: Downstream energy spectrum of protons (blue) and He^{2+} ions (orange) for a simulation with $v_0 = 15v_A$. At low E the Maxwellian distribution is visible. For energies $E \gg T$ the distribution follows a power-law.

In general, the injection efficiency as a function of the shock Mach number exhibits a similar shape for p and He^{2+} . It increases for $M \lesssim 5$ for p , while for He^{2+} an increase up to $M \lesssim 7$ is visible. For higher M the injection efficiency decreases for both species. However, the injection of protons dominates for low Mach number shocks with η_{inj}^p exceeding the value of $\eta_{\text{inj}}^{\text{He}}$ by an order of magnitude. Furthermore, the maximum of the injection efficiency of p shifts towards smaller M compared to He^{2+} . At larger M , the injection efficiency shows the predicted behavior $\eta_{\text{inj}}(M) \sim \ln(M/M^*)/M$ (Eq. (76) in [10]). The prevalence of proton injection at slow shocks is also noticeable in the downstream temperature ratio T_{He}/T_p , which exceeds the expected ratio of four for $M < 15$. This can be explained by the larger fraction of energy which is converted into the energy of the accelerated particles for the protons [20].

4.2 Proton-to-helium ratio

Our aim is now to combine the Mach number dependent injection efficiency with the time dependence of the evolution of a SNR in order to model the time-dependent CR acceleration. It is this combination of injection efficiencies obtained from simulation and the theoretical spectral slope, Eq. (1.3), which allows us to extend the simulation spectra far beyond in rigidity that any simulation may possibly reach. Obviously, this extension is justified because our simulation spectra reach the asymptotic DSA power-law regimes, Fig. 2.

We focus on the Sedov-Taylor phase of the SNR evolution, during which the shock radius increases with time as $R_s \simeq C_{\text{ST}} t^{2/5}$, while the shock velocity decreases as $V_s \simeq (2/5) C_{\text{ST}} t^{-3/5} = (2/5) C_{\text{ST}}^{5/2} R_s^{-3/2}$, with $C_{\text{ST}} \simeq (2E_e/\rho_0)^{1/5}$. Here E_e is the ejecta energy of the supernova and ρ_0 is the ambient density. During the increase of the shock radius from R_{min} to R_{max} , the number of CR particles of species α which are deposited in the shock interior can be calculated as

$$N_\alpha(p) \propto \int_{R_{\text{min}}}^{R_{\text{max}}} f_\alpha(p, M(R)) R^2 dR \propto \int_{M_{\text{max}}^{-2}}^{M_{\text{min}}^{-2}} f_\alpha(p, M) dM^{-2}. \quad (4.2)$$

Here the spectra are represented in the following way:

$$f_\alpha \propto \eta_\alpha(M) (\mathcal{R}/\mathcal{R}_{\text{inj}})^{-q(M)} \quad \text{with} \quad q(M) = 4/(1 - M^{-2}). \quad (4.3)$$

Instead of feeding the simulation data for $\eta_\alpha(M)$ directly to the convolution given by Eqs. (4.2) and (4.3) we take a more practical approach. By fitting the following simple function $\eta_{\text{inj}}(M) = a(M - b)M^{-c}$ to the data extracted from the simulation, we then calculate the proton-to-helium ratio, N_p/N_{He} , according to Eq. (4.2), as a function of rigidity. The results are shown in Fig. 4 by the red line together with the data from the PAMELA and AMS-02 experiments (blue and green shadow areas).

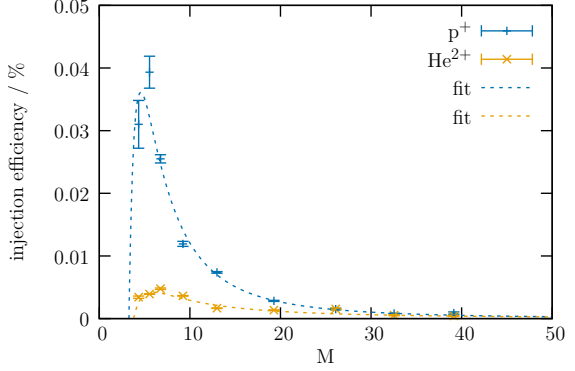


Figure 3: Values for the injection efficiency of protons (blue) and He^{2+} ions (orange) obtained from the simulation according to Eq. (4.1) for different shock velocities.

Our simulations correctly predict the decrease in proton-to-helium ratio with increasing rigidity, shown in Fig. 4, at exactly the rate measured in the experiments, $\Delta q \approx 0.1$, for $\mathcal{R} \gtrsim 10$ GV. Only at lower rigidities, $\mathcal{R} \lesssim 10$ GV, the difference between the data and our predictions becomes noticeable. In fact, some difference has to be expected from Eqs. (1.1) and (1.2), as the rest mass rigidity \mathcal{R}_0 is different for p and He by a factor of two. Based on our discussion in Sec. 1, the difference *must* occur because the equations of motion for p and He deviate towards lower rigidities. Whether the resulting deviation from our prediction based on Eqs. (4.2) and (4.3) comes from the accelerator(s), propagation through the ISM or solar modulation, remains unclear. Except for this uncertainty, the suggested mechanism for A/Z -dependence of the injection fully explains the measured p/He ratio.

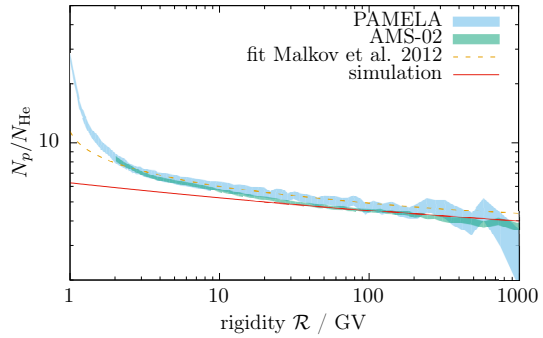


Figure 4: Proton-to-helium ratio as a function of particle rigidity. The results from the simulation (red line) are compared to the PAMELA and AMS-02 data. The observed p/He ratio is accurately reproduced in the range $\mathcal{R} \gtrsim 10$, as expected theoretically (see text).

Acknowledgments

The research was supported by DFG grant TL 2479/2-1, RFBR 16-01-00209, and by NASA ATP-program under grant NNX14AH36G. The authors acknowledge the North-German Supercomputing Alliance (HLRN) for providing the computational resources for the simulations.

References

- [1] O. Adriani *et al.*, *Science* **332**, 69– April (2011).
- [2] M. Aguilar *et al.*, *Physical Review Letters* **115**(21), 211101 (2015).
- [3] Y. S. Yoon *et al.*, *Astrophys. J.* **728**, 122 (2011).
- [4] E. Fermi, *Physical Review* **75**, 1169–1174 (1949).
- [5] AMS-02 Collaboration, <http://www.ams02.org/wp-content/uploads/2016/12/Final.pdf>. (2016).
- [6] M. A. Malkov, *e-prints arXiv:1703.05772* (2017).
- [7] A. E. Vladimirov, G. Jóhannesson, I. V. Moskalenko, and T. A. Porter, *Astrophys. J.* **752**, 68 (2012).
- [8] Y. Ohira and K. Ioka, *Astrophys. J. Lett.* **729**, L13+ (2011).
- [9] Y. Ohira, N. Kawanaka, and K. Ioka, *Phys. Rev. D* **93**(8), 083001 (2016).
- [10] M. A. Malkov, *Phys. Rev. E* **58**, 4911–4928 (1998).
- [11] M. A. Malkov and H. J. Völk, *Astronomy and Astrophys.* **300**, 605–626 (1995).
- [12] M. A. Malkov and H. J. Völk, *Advances in Space Research* **21**, 551–554 (1998).
- [13] M. A. Malkov, P. H. Diamond, and R. Z. Sagdeev, *Physical Review Letters* **108**(8), 081104 (2012).
- [14] D. Burgess, *Geophys. Res. Lett.* **16**, 163–166 (1989).
- [15] K. J. Trattner and M. Scholer, *Geophys. Res. Lett.* **18**, 1817–1820 (1991).
- [16] D. Caprioli, D. T. Yi, and A. Spitkovsky, *ArXiv e-prints* (2017).
- [17] G. M. Zaslavsky, *Physics of chaos in Hamiltonian systems*. (2007).
- [18] T. V. Liseykina *et al.*, *Journal of Plasma Physics* **81** 10 (2015).
- [19] M. A. Malkov *et al.*, *Physics of Plasmas* **23**(4) (2016).
- [20] U. D. J. Gieseler, T. W. Jones, and H. Kang, *Astronomy and Astrophys.* **364**, 911–922 (2000).